Heliyon 10 (2024) e24077

Contents lists available at ScienceDirect

Heliyon

journal homepage: www.cell.com/heliyon

Research article

Host-guest interactions of coumarin-based 1,2-pyrazole using analytical and computational methods: Paper strip-based detection, live cell imaging, logic gates and keypad lock applications

Puthiyavalappil Rasin [a], Sabeel M. Basheer [a,b], Jebiti Haribabu [c,d], K.N. Aneesrahman [a], Vipin Manakkadan [a], Vishnunarayanan Namboothiri Vadakkedathu Palakkeezhillam [a], Nattamai Bhuvanesh [e], Cesar Echeverria [c], Juan F. Santibanez [f,g], Anandaram Sreekanth [a,*]

[a] Department of Chemistry, National Institute of Technology-Tiruchirappalli, Tamil Nadu, 620015, India
[b] Dr. Sabeel M Basheer, Department of Chemistry, School of Advanced Sciences, VIT-AP University, 522 237, Andhra Pradesh, India
[c] ATACAMA-OMICS, Facultad de Medicine, Universidad de, Los Carreras 1579, 1532502, Copiapo, Chile
[d] Chennai Institute of Technology (CIT), Chennai 600069, India
[e] Department of Chemistry, Texas A & M University, College Station, TX 77842, USA
[f] Institute for Medical Research, National Institute of the Republic of Serbia, University of Belgrade, Belgrade, Serbia
[g] Integrative Center for Biology and Applied Chemistry (CIBQA), Bernardo O'Higgins University, Santiago, Chile

ARTICLE INFO

Keywords:
Chemosensor
NBO
DFT
Logic gates
Keypad lock

ABSTRACT

A novel Coumarin-based 1,2-pyrazole, HCPyTSC is synthesised and characterized. The chemosensor has been shown to have efficient colourimetric and fluorescence sensing capabilities for the quick and selective detection of fluoride and copper ions. At 376 and 430 nm, the HCPyTSC exhibits selective sensing for Cu^{2+} and F^- ions. By examining the natural bond orbital (NBO) analysis and the potential energy curve (PES) of the ground state for the function of the C–H bond, it has been determined from the theoretical study at hand that the deprotonation was taken from the 'CH' proton of the pyrazole ring. For F^- and Cu^{2+}, the HCPyTSC detection limits were 4.62 nM and 15.36 nM, respectively. Similarly, the binding constants (Kb) for F^- and Cu^{2+} ions in acetonitrile medium were found to be 2.06×10^5 M^{-1} and 1.88×10^5 M^{-1}. Chemosensor HCPyTSC with and without F^- and Cu^{2+} ions have an emission and absorption response that can imitate a variety of logic gates, including the AND, XOR, and OR gates. Additionally, a paper-based sensor strip with the HCPyTSC was created for use in practical, flexible F^- sensing applications. The paper-based sensor was more effective in detecting F^- than other anions. The effectiveness of HCPyTSC for the selective detection of F^- in living cells as well as its cell permeability were examined using live-cell imaging in T24 cells.

* Corresponding author.
E-mail address: sreekanth@nitt.edu (A. Sreekanth).

https://doi.org/10.1016/j.heliyon.2024.e24077
Received 4 August 2023; Received in revised form 19 December 2023; Accepted 3 January 2024
Available online 5 January 2024

1. Introduction

Copper is the third most abundant transition element in living creatures and it is found naturally in soil, rock, water, sediment and air [1]. This increased occurrence, along with its peculiar thermo-electric characteristics, makes it extremely useful in a variety of sectors, including alloys, machine components, batteries, electric wires, fertilisers, and so on [2–4]. Similarly, it plays an important part in many biological processes such as metabolic control, connective tissue creation, protection from fungal and yeast infections, and maintaining oestrogen metabolism in women [5–7]. Copper may be found in a variety of foods, including shellfish, nuts, seeds, grain goods, wheat bran cereals, organ meats and cocoa products [8]. Copper-based medications have been recommended for patients undergoing intestinal bypass surgery, anaemia, wound healing, brittle bones (osteoporosis), and osteoarthritis [9–11]. Copper insufficiency and overload in the live body might raise the risk of numerous ailments. Its deficiency, for example, can result in anaemia-like symptoms as well as hypopigmentation and bone deformities [12–14]. Overloading of copper, can cause Wilson's disease, prion disease and Alzheimer's disease [15–17]. Copper compounds are harmful to bacteria and viruses and are widely employed in water treatment and as wood and leather preservatives [18,19]. As a result, the environmental impact of copper cannot be overlooked. To avoid any negative health impacts, the WHO recommends that copper ions concentrations in drinking water be less than 2 ppm[20]. It is crucial to create extremely focused, sensitive, and precise sensors in order to find traces.

Since fluoride is a naturally occurring element of the environment, it is always a part of people's daily lives. Food, air, and things containing fluoride are all ways that fluoride enters the body [20]. Fluoride plays a key role in maintaining the strength of our bones and teeth [21,22]. Fluoride is essential for the development of our teeth since it helps to fortify our tooth enamel as it grows and develops. Including any other substance, we come into contact with on a daily basis (like oxygen, water, and table salt), fluoride can be dangerous in certain doses. The first organ to be impacted is the stomach [23]. The initial symptoms and indicators include nausea, stomach pain, violent vomiting, and diarrhoea. After that, the person collapses with symptoms such as weakness, paleness, shallow breathing, weak heartbeats, damp, cold skin, cyanosis, dilated pupils, hypocalcaemia, and hyperkalaemia [24–26]. In two to 4 h, the person may potentially pass away. Consequently, keeping the right quantity of fluoride ions in the environment can help to prevent fluoride poisoning, which highlights the importance of creating low-cost fluoride sensors. Because of the fluoride ion's small size, high electron density, and large electronegativity, chemosensors frequently form strong hydrogen bonds with it [27,28]. The hydroxyl, amine and hydrogen attached to electron-deficient atoms are quite well in forming hydrogen bonds in anion sites [29]. These characteristics of fluoride ions could be useful in the design and creation of novel fluoride sensor series.

To create and construct better fluorescence sensors for ions, it is crucial to understand the theoretical side of the chemosensing mechanism. Because of the great biocompatibility, robust and steady fluorescence emission, and remarkable structural flexibility, the coumarin platform has more recently been widely used in the construction of small-molecule fluorescent chemosensors. The C═C bond is fixed in the *cis*-conformation, which helps prevent the *trans*-cis transition of typical C═C bonds in vinylic compounds and contributes to the high fluorescence emission and good photostability of coumarins. Due to quenching processes like the photoinduced electron transfer (PET), isomerization, and other factors, some coumarin derivatives are weak fluorophores. These quenching effects are suppressed and a bright fluorescence is regained after interactions with their analytes [30,31].

Here, we report the synthesis of coumarin-based 1,2-pyrazole chemosensor that can be used to detect F^- and Cu^{2+} ions with the naked eye. The sensing mechanism is explained in detail by using spectroscopic methods and theoretical investigations. Also, we described the multiple logic gate operations of the synthesised ligand along with their molecular keypad applications.

2. Experimental section

2.1. Materials and methods

On a Bruker, 500 MHz in DMSO-d_6 at 298 K, with TMS as an internal standard, the ^1H and ^{13}C NMR spectra were generated. Using a Perkin-Elmer FT-IR spectrophotometer in the 400–4000 cm^{-1} range, the HCPyTSC powder was examined. An Agilent mass spectrometer was used to examine the mass spectra of HCPyTSC. UV–Vis diode-array spectrometer (Analytical Jena Specords 600) was used to create UV–Vis absorption spectra, and a spectrofluorometer (Jasco V-630) fitted with a xenon discharge lamp in a 1 cm quartz cell with a 5 nm slit width was utilised to create and analyse emission spectra. At 298 K, all measurements were made. Utilizing the software Origin 8.5, the fluorescence titration data was gathered and spectra were generated. The chemosensor was created using 4-hydroxy-2-oxo-2H-1-benzopyran-3-carboxaldehyde and N(4)-pyrrolidine thiosemicarbazide, and its sensing properties were investigated using a variety of metal chlorides, including Co^{2+}, Fe^{2+}, Pb^{2+}, Fe^{3+}, Ni^{2+}, Mg^{2+}, Cd^{2+}, Al^{3+}, Mn^{2+}, Ca^{2+}, Ga^{3+}, Cr^{3+}, Hg^{2+}, Zn^{2+},

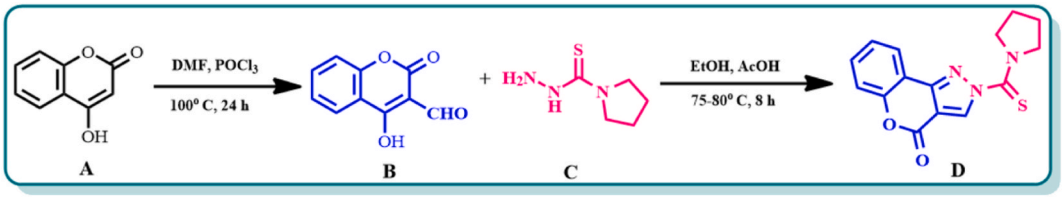

Scheme 1. Synthesis of chemosensor HCPyTSC.

Cu^{2+} and tetrabutyl ammonium salts of F^-, CN^-, Cl^-, Br^-, I^-, ClO_4^-, $H_2PO_4^-$, HSO_4^-, OH^- and AcO^-.

2.2. Synthesis of HCPyTSC

By refluxing 4-hydroxycoumarin (A) with dimethyl formamide and phosphorous oxychloride, 4-hydroxy-2-oxo-2H-1-benzopyran-3-carboxaldehyde (B) has been created using the Vilsmeier Haack reaction [32]. Compound B, after being dissolved in ethanol (30 mL), N(4)-pyrrolidine thiosemicarbazide (0.290 g, 2 mmol) (C) was added to the reaction mixture. A few drops of acetic acid were added, and the mixture then refluxed for 8 h. At room temperature, the reaction mixture was left alone to gradually evaporate. The generated product [(pyrrolidine-1-carbonothioyl) chromeno [4,3-c] pyrazol-4(2H)-one] (HCPyTSC) (D)) was separated following evaporation. Additionally, the product was vacuum-dried after recrystallization from a 1:1 combination of chloroform and ethanol (Scheme 1).

2.3. Single crystal X-ray crystallography

A good yellow block with very well-defined faces and dimensions (max, intermediate, and min) of $0.102 \times 0.067 \times 0.037$ mm^3 was found in a representative sample of crystals using a Leica MZ 75 microscope. A cold nitrogen stream (Oxford) sustained at 150 K was then used to submerge the crystal attached to a nylon loop. The unit cell determination, data collection, and crystal screening were all done using a BRUKER APEX 2 X-ray (three-circle) diffractometer. The APEX2 software suite, version 2008–6.0, was used to control the goniometer [33]. The sample was optically centred with the aid of a camera so that no translations could be observed when the crystal rotated through all of its orientations. The detector (APEX2, 512 512 pixels) was positioned 6.0 cm away from the crystal. The X-rays used were produced using a Mo sealed X-ray tube with a voltage of 40 kV and a current of 40 mA (K = 0.70173). Sixty data frames with 1.0° widths were collected. The auto-indexing process identified the unit cell using these reflections. Nonlinear least squares and Bravais lattice methods were used to identify and improve a suitable cell. The unit cell was examined by looking at the h k l overlays on different data frames. There were no super-cells or false reflections found. After thoroughly inspecting the unit cell, a lengthy data gathering operation (4 sets) utilizing omega scans was started. Utilizing XT/XS in APEX2, a solution was quickly attained [34]. The hydrogen atoms were set up in hypothetical positions and mounted on their corresponding parent atoms. Anisotropic thermal parameters were used to optimise each and every non-hydrogen atom. Using PLATON, the lack of further symmetry and voids was confirmed (ADDSYM). Weighted least squares refinement on F2 was used to further enhance the structure. Table 1 includes a list of the dimensions and additional parameters.

2.4. UV–vis and fluorescence spectral studies

HCPyTSC (10 μM) stock solution was prepared in acetonitrile. Stock solutions of tetrabutyl ammonium salts of F^-, CN^-, Cl^-, Br^-, I^-, ClO_4^-, $H_2PO_4^-$, HSO_4^-, OH^- and AcO^- and some common metal cations including first-row transition metal ions (Co^{2+}, Fe^{2+}, Pb^{2+}, Fe^{3+}, Ni^{2+}, Mg^{2+}, Cd^{2+}, Al^{3+}, Mn^{2+}, Ca^{2+}, Ga^{3+}, Cr^{3+}, Hg^{2+}, Zn^{2+}, Cu^{2+}) were prepared in water. The UV–Visible and fluorescence spectra of the chemosensor were recorded at room temperature after the addition of different concentrations of anions and cations solutions.

2.5. CV titration

The electrochemical behavior of the chemosensor was monitored by cyclic voltammetry. To perform this study, the chosen ions were titrated with the chemosensor HCPyTSC in acetonitrile with 0.1 M tetra-butyl ammonium perchlorate as a supporting electrolyte. Using glassy carbon as the working electrode and platinum wire as the counter electrode, the redox potentials of the HCPyTSC were measured using cyclic voltammetry at a scan rate of 0.1 mV/s.

2.6. ^1H NMR titration

The HCPyTSC (1 Mm/L in DMSO-d_6) was titrated with fluoride ions. The tetrabutylammonium salt solution with a concentration of (1 Mm/L) is used to generate the fluoride anion. Fluoride titration was carried out by the incremental addition of fluoride anion to the HCPyTSC molecules.

Table 1
Selected bond length, bond angle and torsion angle for HCPyTSC.

Bond length (Å)	Bond angle (°)	Torsion angle (°)
S(1)–C(11) 1.6703	C(3)-N(1)-N(2) 103.32	N(1)-N(2)-C(11)-S(1) 149.76
N(2)–N(1) 1.3825	N(2)-C(10)-C(4) 105.74	C(11)-N(2)-N(1)-C(3) −176.18
N(2)–C(10) 1.3574	N(2)-C(10)-H(10) 127.1	C(11)-N(2)-C(10)-C(4) 176.21
N(2)–C(11) 1.4324	N(2)-C(11)-S(1) 118.84	C(12)-N(3)-C(11)-S(1) 165.63
N(3)–C(11) 1.3181	N(3)-C(11)-S(1) 124.61	C(15)-N(3)-C(11)-S(1) −5.28

2.7. pH study

The effect of pH on Cu^{2+} and F^- ion sensing was investigated over the pH window from 2 to 12. The medium's pH was controlled using sodium hydroxide solution and hydrochloric acid. The chemosensor HCPyTSC (2.49 mg, 1×10^{-3} M) was dissolved in acetonitrile (10 mL) after which 30 μL of this solution was diluted to the appropriate pH solutions (3 mL). For each of the chemosensor solutions prepared earlier an additional amount of 30 μL of 1 mM Cu^{2+} and F^- ions were added. After thorough mixing, fluorescence spectra were captured at room temperature.

2.8. Live cell image studies

The applicability of the chemosensor HCPyTSC to sense F^- ions in organ systems was examined using fluorescence imaging. Using the MTT (3-(4,5-dimethylthiazol-2-yl)-2,5-diphenyl-2H-tetrazolium bromide) test methodology, cell toxicity was evaluated prior to this experiment [35–39]. The T24 cells were exposed to various doses of the chemosensor HCPyTSC for 12 h prior to the test (0–50 μM). In 12-well plates with complete media, T24 cells were seeded and grown for 12 h at 37 °C with 5 % CO_2. The cells were extensively rinsed with phosphate buffer solution to eliminate extra F^- ions (PBS). HCPyTSC (10 μM) was then applied to the cells for 10 min. After that, the cells were completely and delicately rinsed with PBS to get rid of any leftover culture medium and HCPyTSC. The cell images were taken with a fluorescence microscope after the cells were fixed in a 3.7% formaldehyde solution (pH 7.0).

2.9. Computational method

Gaussian 09 programme was used to complete all the theoretical calculations. To have a better insight into the electronic spectra and electronic excited state, the DFT and TD-DFT calculations were performed. The geometry optimizations for the ground state were carried out using the hybrid functional B3LYP and 6-311G(d,p) basis set, which is reasonable and suitable for such massive organic compounds. Since the experiments were carried out in acetonitrile solvent, the computational predictions have been done by using the polarizable continuum model (PCM), which has an acetonitrile-specific dielectric constant of 37.5. The CAM B3LYP/6-311G(d,p) level was employed for the TD-DFT analysis, and the B3LYP/LanL2DZ level was used for the chemosensor-Cu^{2+} complex [40]. To determine the mechanism of the sensing, transition state (TS) and intrinsic reaction coordinate (IRC) computations were performed. The vibrational frequency analysis validated the local minima in the ground state, transition state, intermediate state, and excited state. Natural bond orbital (NBO) analysis was used to compute the charge distribution, occupancy, and energy of the bonding orbitals at the same theoretical level as the ground state and excited state geometry-optimized structures of the chemosensor- F^- complex. To assess the donor-acceptor interaction, the second-order perturbation energies of the chemosensor- F^- was calculated. To validate the sensing mechanism, potential surface curve (PES) assessments were also performed.

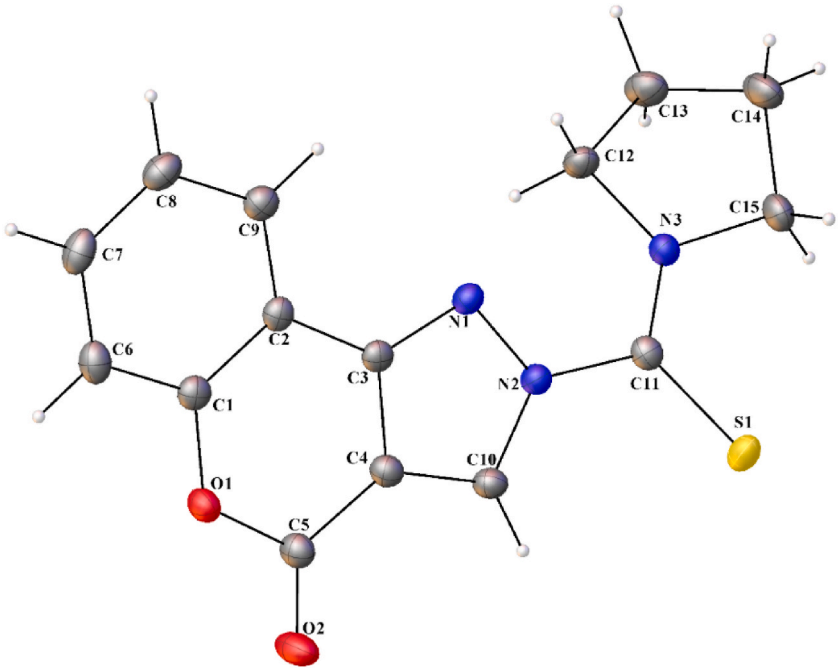

Fig. 1. Molecular structure of HCPyTSC with the labelling of selected atoms.

3. Results and discussion

3.1. Synthesis

The HCPyTSC was synthesised via Schiff's base condensation reaction of N(4)-pyrrolidine thiosemicarbazide and appropriate aldehyde (4-hydroxy-2-oxo-2H-1-benzopyran-3-carboxaldehyde). It was thoroughly characterized by FT-IR, ^{1}H NMR, ^{13}C NMR, and MASS spectra before being employed in sensing and other practical applications. Using FT-IR spectroscopy, we determined the presence of functional groups like C═S, C═O, C═N etc. by looking at the absorption peak that results from the stretching vibrations of the bonds in the functional groups. Sharp peaks at 1728, 1669 and 1180 cm^{-1} indicate the existence of (C═O), (C═N) and (C═S) groups in the HCPyTSC correspondingly. One of the key methods for determining the structural details of molecules is NMR spectroscopy. The only proton presented in the pyrazole ring is clearly represented by the sharp singlet at 9.25 in the ^{1}H NMR of HCPyTSC. HCPyTSC's aromatic ring protons exhibit doublets and triplets at about δ 8.07–7.42 ppm. Whereas the triplets and multiplets around the region δ 3.87–2.03 ppm correspond to the CH_2 protons present in the pyrrolidine ring. The well-defined peaks in the ^{13}C NMR spectra correspond to the thione carbon (C═S), C═O carbon, and azomethine (C═N) groups and are located at 173.63, 156.88, and 153.32 ppm respectively. The benzene aromatic carbons were discovered multiplets at ppm 136.38, 125.42–114.19 ppm. The nitrogen-attached pyrrolidine carbon was measured at 55.99 and 54.66 ppm. All the characterization spectra and their detailed description were summarized in the supplementary material (Figs. S2, S4, S5 and S6).

3.2. Single crystal X-ray crystallography

Fig. 1 shows the molecular structure of the HCPyTSC along with atom numbering and molecular packing. Table 1 contains information about the crystal data as well as specific interatomic bond lengths, angles, torsion angles, and hydrogen bonding. With dimensions (max, intermediate, and min) 0.102 × 0.067 × 0.037 mm^3 from a representative, the HCPyTSC exhibits a monoclinic P121/c1 space group and produces an appropriate yellow block with extremely well-defined faces. In relation to the C(11)–N(2) bond, the sulphur atom S(1) and the hydrazone nitrogen N(1) are in the *E* position. Moreover, the N(1)–N(3) bond lengths in the chemosensor HCPyTSC are intermediate between ideal values of the corresponding single [N–N, 1.45 Å; C–N, 1.47 Å] and double bonds [N═N, 1.25 Å; C═N, 1.28 Å], providing evidence for an extended-delocalization along the N_1–N_2–C_{11}–S_1 chain.

3.3. UV–vis and fluorescence spectral studies

In acetonitrile solution, colourimetric analysis was used to examine the interactions of the HCPyTSC with a variety of anions, including F^-, CN^-, Cl^-, Br^-, I^-, ClO_4^-, $H_2PO_4^-$, HSO_4^-, OH^- and AcO^-, and first transition metal ions, including Co^{2+}, Fe^{2+}, Pb^{2+}, Fe^{3+}, Ni^{2+}, Mg^{2+}, Cd^{2+}, Al^{3+}, Mn^{2+}, Ca^{2+}, Ga^{3+}, Cr^{3+}, Hg^{2+}, Zn^{2+} and Cu^{2+}. HCPyTSC had a significant and perceptible colour change with the addition of fluoride and copper ions, taking on hues of dark yellow and light yellow, respectively (Fig. S1). There were no apparent colour changes with the addition of more anions and cations. The UV–Vis spectra have been recorded in the acetonitrile solvent at room temperature. The peaks at 325 and 372 nm for HCPyTSC confirm the presence of the π -π* and n-π* transitions respectively [41]. Additionally, TD-DFT results give more insights into the transitions. The band around 325 might be due to the excitation of electrons from the ground singlet state to the third singlet excited state (S3). Similarly, the band around 372 nm is attributed to a transition from the ground singlet state to the second singlet excited state (S2). For the n-π* transition, n orbital is delocalized over both pyrazole and thiourea subunits, and π* orbital is located mainly at the coumarin subunit (Fig. S7). Figs. S8 and S10 demonstrate that adding cations

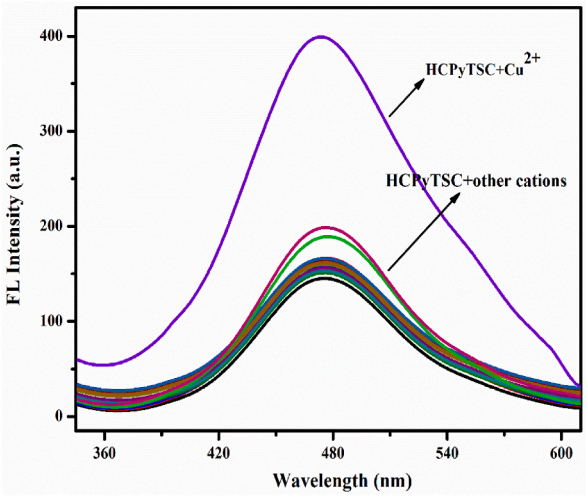

Fig. 2. HCPyTSC (1 × 10^{-5} M) fluorescence emission pattern in acetonitrile with different metal ions (1 × 10^{-3} M), λex = 372 nm, λem = 476 nm.

and anions to the HCPyTSC didn't produce any change in the UV–Vis spectra except for copper and fluoride ions. The addition of fluoride ions to the HCPyTSC led to the emergence of a new broad peak at 430 nm. The new broad peak that has formed indicates the presence of the HCPyTSC-F^- complex and a hydrogen bond between the host and guest molecules. The newly created band in the visible range exhibits the hyperchromic shift with the addition of fluoride ion. During the presence of copper ion, the peak at 376 nm almost disappeared as a result of lone pair electron engagement in complex formation. The changes observed in the absorption spectra of HCPyTSC upon the addition of F^- and Cu^{2+} are due to the charge transfer from the ligand to the guest species.

Similar to the UV–Vis study, fluorescence measurements were conducted to understand more about the receptor's sensing capacity. Furthermore, fluorescence emission spectroscopy is a better method for anion sensing than absorption spectroscopy. Prior to beginning the fluorescence measurements, depending on the sensor's absorption wavelength, the excitation wavelength was chosen to be 372 nm. In an acetonitrile solution, the sensor HCPyTSC was examined for its ability to sense several metal cations, including chloride salts of Co^{2+}, Fe^{2+}, Pb^{2+}, Fe^{3+}, Ni^{2+}, Mg^{2+}, Cd^{2+}, Al^{3+}, Mn^{2+}, Ca^{2+}, Ga^{3+}, Cr^{3+}, Hg^{2+}, Zn^{2+}, Cu^{2+} and anions such as F^-, CN^-, Cl^-, Br^-, I^-, ClO_4^-, $H_2PO_4^-$, HSO_4^-, OH^- and AcO^-. Figs. 2 and 4 show the HCPyTSC sensor's fluorescence spectrum shifts when different metal cations and anions are involved. Fluorescence amplification occurred at 476 nm and 492 nm when copper and fluoride ions were added separately to HCPyTSC. Whereas other metal cations and anions failed to impart any significant changes in the fluorescence spectra of the sensor HCPyTSC with Cu^{2+} and F^- (Figs. 3 and 5). These findings described that the sensor HCPyTSC has the least binding affinity for the other metal cations and anions under study and the best binding affinity for Cu^{2+} and F^-. Copper and fluoride ions can be effectively differentiated by analyzing their emission wavelengths and the shape of their respective emission spectra. In the case of the HCPyTSC-Cu^{2+} complex, it exhibits emission at approximately 476 nm, whereas the HCPyTSC-F- complex displays a distinctive peak at 492 nm. Notably, the fluoride complex of the sensor presents a unique emission spectrum characterized by a broad peak with a discernible shoulder. These distinct emission patterns allow for clear differentiation between copper and fluoride ions, even when both are present in the same sample.

To gain a deeper knowledge of the molecular interaction between the sensor HCPyTSC, Cu^{2+} and F^- ions, fluorescence titration studies were conducted. As shown in Fig. 6, the fluorescence emission intensity gradually rose after Cu^{2+} and F^- ions were incrementally added to HCPyTSC in an acetonitrile solution. Upon the addition of F^- from 0 to 1 equivalents to the HCPyTSC solution, the fluorescence emission intensity increased gradually with a shift in emission wavelength from 476 nm to 492 nm. While the peak position was unaffected by the progressive increase in fluorescence intensity caused by the incremental addition of Cu^{2+} ions. Fluoride in combination with HCPyTSC causes fluorescence enhancement, which links the relaxation from the stimulated state to the PET process. The presence of a strong intramolecular hydrogen bond between C10···H···F may possibly contribute to the fluorescence increase. At higher concentrations (above 1 Equiv.) the saturation of complexation with the of Cu^{2+} and F^- ions stopped the increase in emission intensities (see Fig. 7).

The modified Benesi-Hildebrand equation (Equation (1)), was used to calculate the binding constant.

$$\frac{1}{(F_X\text{-}F_0)} = \frac{1}{(F_\infty\text{-}F_0)} + \frac{1}{K[C]((F_\infty\text{-}F_0))} \tag{1}$$

Where F_0 and Fx are the corresponding emission intensities of the receptor when it is acting alone and when ions are added, respectively. "K" stands for the association constant, and "C" stands for the increased ion concentration. The plot of $1/(Fx\text{-}F_0)$ vs $1/[C]$ was used to compute the association constants. The ratio of intercept/slope was used to calculate the binding constant of the sensor HCPyTSC towards F^- and Cu^{2+}, and the results showed that it is 2.06105 M^{-1} and 1.88105 M^{-1}, respectively (Fig. 8B and C). It is

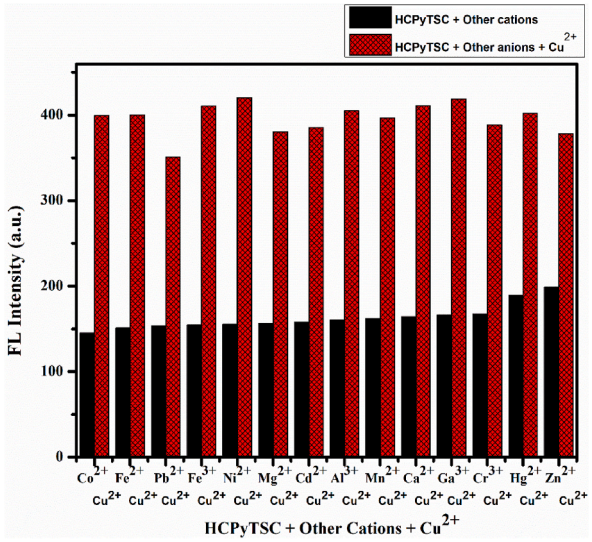

Fig. 3. Competitive analysis of the HCPyTSC-Cu^{2+} sensor against several metal ions in acetonitrile solution, λex = 372 nm, λem = 476 nm.

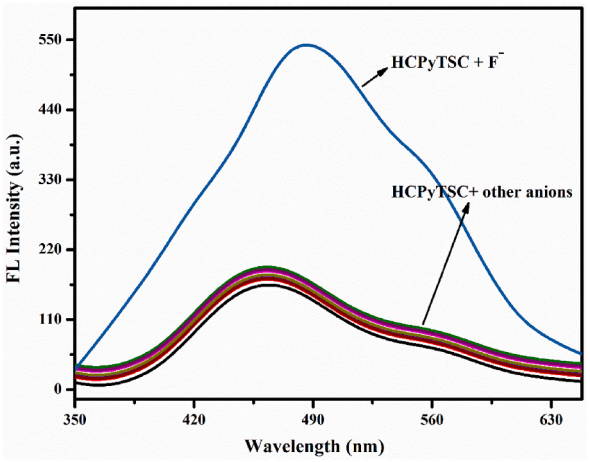

Fig. 4. Emission pattern of the HCPyTSC (1×10^{-5} M) in acetonitrile with various anions (1×10^{-3} M), λex = 372 nm, λem = 492 nm.

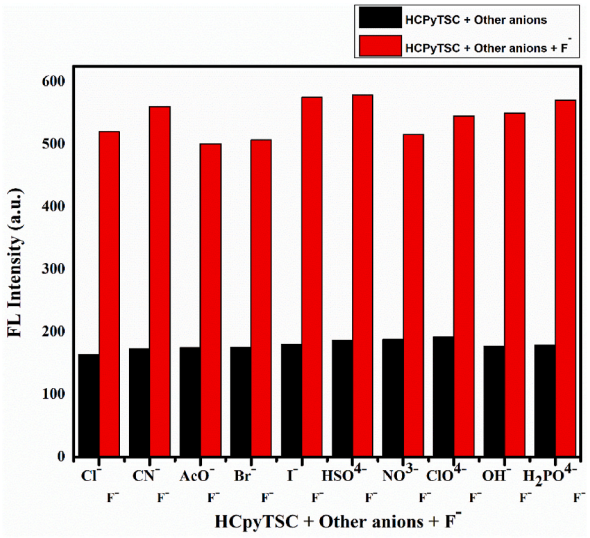

Fig. 5. Competitive analysis of the HCPyTSC-F^- sensor against several anions in acetonitrile solution, λex = 372 nm, λem = 492 nm.

obvious from the values of the binding constants that F^- has a higher fluorescence binding affinity towards HCPyTSC than Cu^{2+}. Using equation 3 σ/K and the calibration curve of the emission data, the detection limits of the sensor HCPyTSC were calculated. The value of 4.62 nM and 15.36 nM were discovered to be the detection limits for F^- and Cu^{2+}. At 476 nm and 492 nm, stronger linear correlations were seen ($R^2 = 0.9932$ and 0.9954) illustrating a better linear correlation for the detection of Cu^{2+} and F^- ions. Using the Job plot method, the binding stoichiometry between HCPyTSC-Cu^{2+} and HCPyTSC-F^- was assessed. In an acetonitrile medium, identical quantities of the sensor HCPyTSC, Cu^{2+}, and F^- were added. The concentration of HCPyTSC varied from 0.1×10^{-5} M to 1×10^{-5} M. The greatest emission intensity was seen at 0.5 mol fractions (Fig. 8A), as shown by Job's plot, proving a 1:1 ratio between the HCPyTSC-Cu^{2+} and HCPyTSC-F^- complexes.

3.4. Reversibility of the sensor HCPyTSC

Since it is crucial when we examine the sensor's applications in the fields of sensing and bioimaging, we further looked into the reversibility behavior of the HCPyTSC sensor. By adding EDTA (2.0×10^{-3} M), the HCPyTSC-Cu^{2+} complex (1×10^{-5} M^{-1} - 1×10^{-3} M) in acetonitrile solution was reversed. After the addition of EDTA, the Cu^{2+} complex formation with the sensor HCPyTSC vanished (Fig. S12), demonstrating the reversibility of the sensing action.

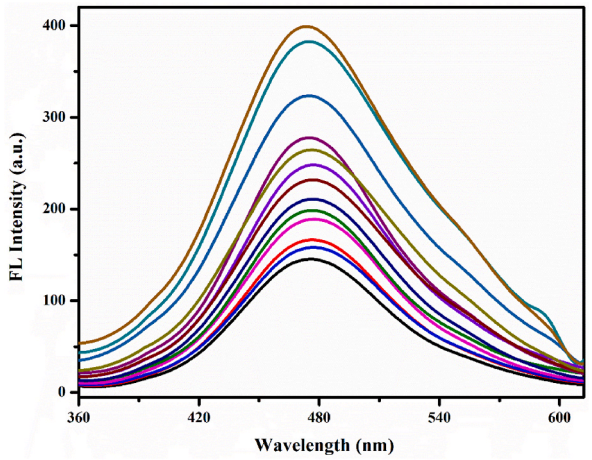

Fig. 6. Emission spectra of HCPyTSC (1×10^{-5} M) after adding Cu^{2+} in small amounts in an acetonitrile solution (λex = 372 nm, λem = 476 nm).

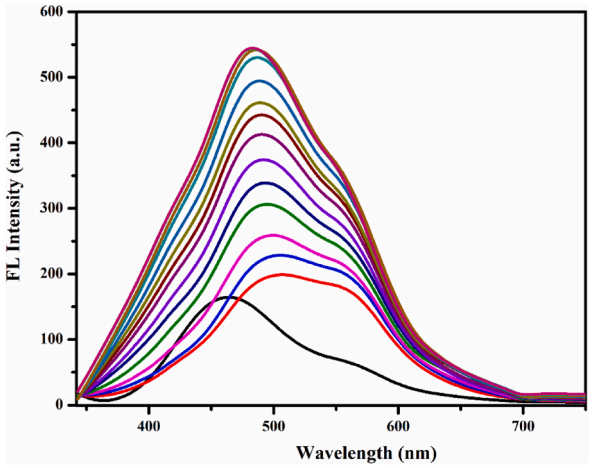

Fig. 7. FL emission spectra of HCPyTSC (1×10^{-5} M) after adding F^- in small amounts in an acetonitrile solution (λex = 372 nm, λem = 492 nm).

3.5. Time-dependence study

Fluorescence spectrophotometry was also used to conduct a time-dependence analysis in order to use the sensor HCPyTSC for practical Cu^{2+} and F^-ion sensing applications. In order to conduct this investigation, Cu^{2+} and F^- ions were added to the sensor HCPyTSC, and fluorescence spectra were taken at regular intervals (0–200 s) (Fig. S13). The findings showed that the fluorescence intensity did not significantly change across different time periods, suggesting that HCPyTSC might be used as a quick tool for the detection of Cu^{2+} and F^- ions with a response time of 30 s.

3.6. pH study

By adjusting the medium's pH using sodium hydroxide and hydrochloric acid, the pH conditions of the chemosensors HCPyTSC, HCPyTSC–Cu^{2+} and HCPyTSC-F^- were examined for real-time applications. Copper and fluoride sensing with the HCPyTSC sensor has been effectively conducted within the pH range of 7–8, aligning well with the typical pH range found in most biological systems. Fig. S14 depicts changes in the chemosensor HCPyTSC, HCPyTSC–Cu^{2+} and HCPyTSC-F^-'s fluorescence intensity at varied pH levels between 1 and 12. The sensor exhibits higher emission in acidic and neutral mediums describing the protonation of heteroatoms in the sensor as well as the HCPyTSC-Cu^{2+} complex formation that could hinder the charge transfer within the sensor. In contrast, the fluorescence intensity falls in basic media, which may be caused by the lack of Cu^{2+} needed for complex formation as a result of copper hydroxide production [42]. Similar to this, the combination of HCPyTSC and fluoride ion results in reduced intensity in acidic medium, while increasing the emission in neutral and basic environments.

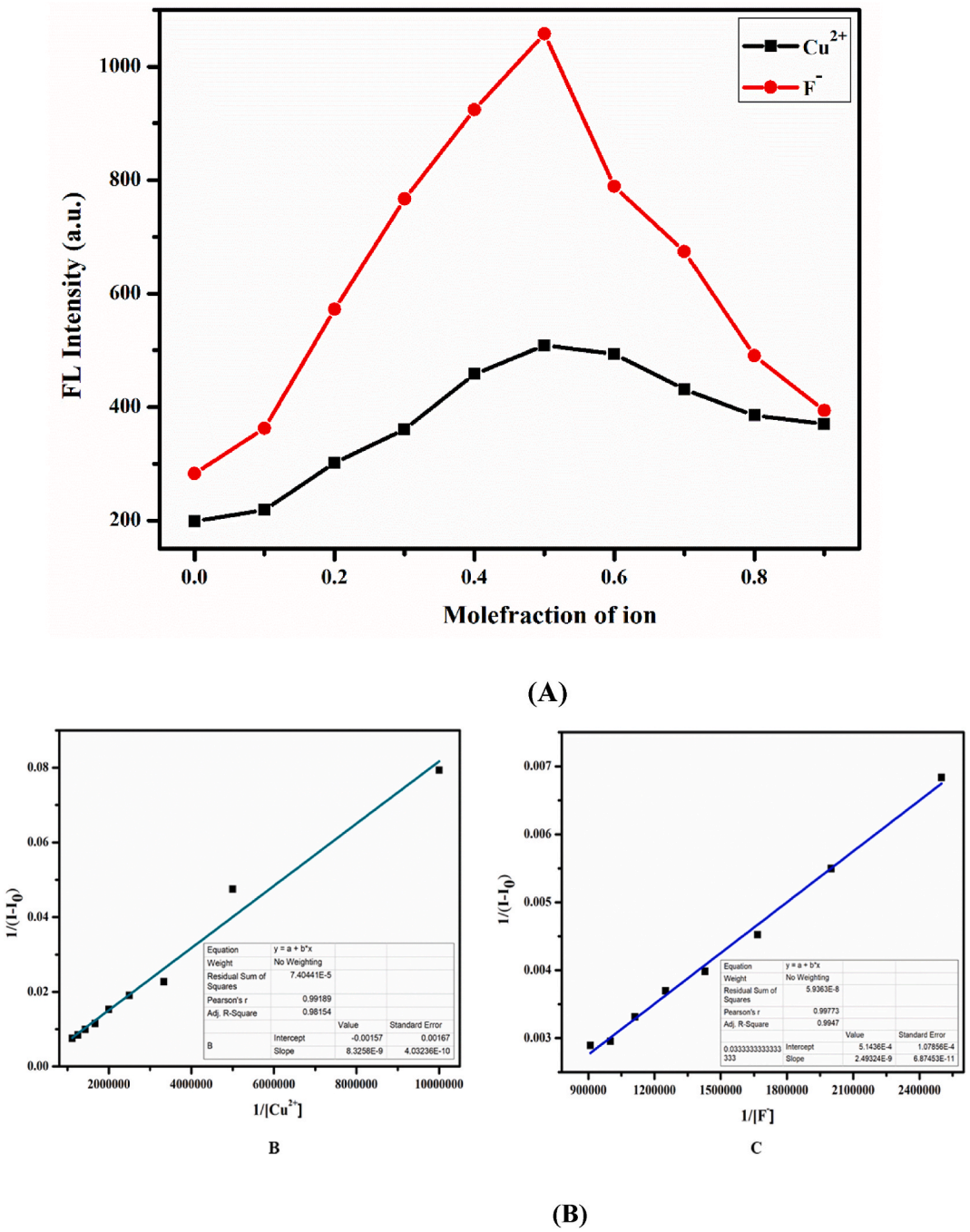

Fig. 8. Job's plot (A) and Benesi-Hildebrand plot of HCPyTSC with copper (B) and fluoride ions (C) λex = 372 nm, λem = 476/492 nm.

3.7. IR spectral analysis

To thoroughly comprehend the complex formation mechanism of HCPyTSC with Cu^{2+} metal ions, FT-IR spectral study was carried out. The IR peak of the carbonyl C═O group (1728 cm^{-1}), imine C═N (1669 cm^{-1}), and thiocarbonyl C═S group (1180 cm^{-1}) arosed in the foreseen positions, as shown in Fig. 9. Even after the addition of Cu^{2+} ions, no discernible alteration in the peak of C═O moiety was seen. It blatantly implies that there is no interaction between the carbonyl group in the sensor HCPyTSC and the Cu^{2+} ions. While the stretching frequency of the imine moiety has a noticeable blue shift from 1669 cm^{-1} to 1621 cm^{-1}. Additionally, the consecutive additions of Cu^{2+} result in a decrease in the intensity of the C═N group. Similarly, the peak associated with the thiocarbonyl group shifted from 1180 cm^{-1} to 1162 cm^{-1} with the consecutive addition of Cu^{2+} ions. The findings indicated a potential for Cu^{2+}

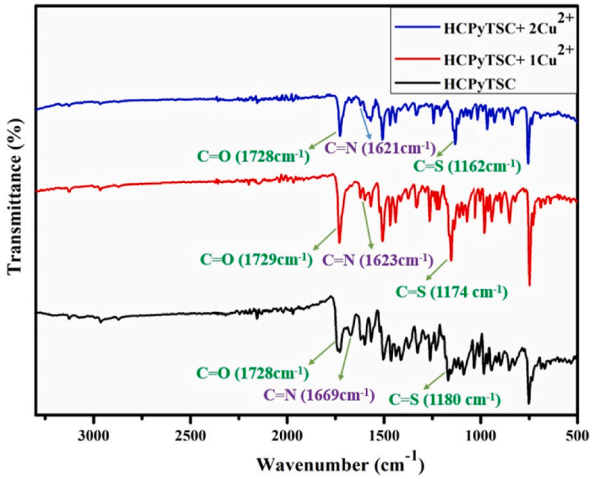

Fig. 9. FT-IR spectra of HCPyTSC and HCPyTSC–Cu^{2+} (1:1) complex.

coordination with imine C═N and C═S moieties.

3.8. NMR titration

To better comprehend the detecting mechanism, ^{1}H NMR titration for the sensor in DMSO-d_6 with and without F^{-} ion was conducted. The single peak at 9.25 ppm in the case of pure HCPyTSC clearly shows that there is only one proton (C10–H10) in the pyrazole

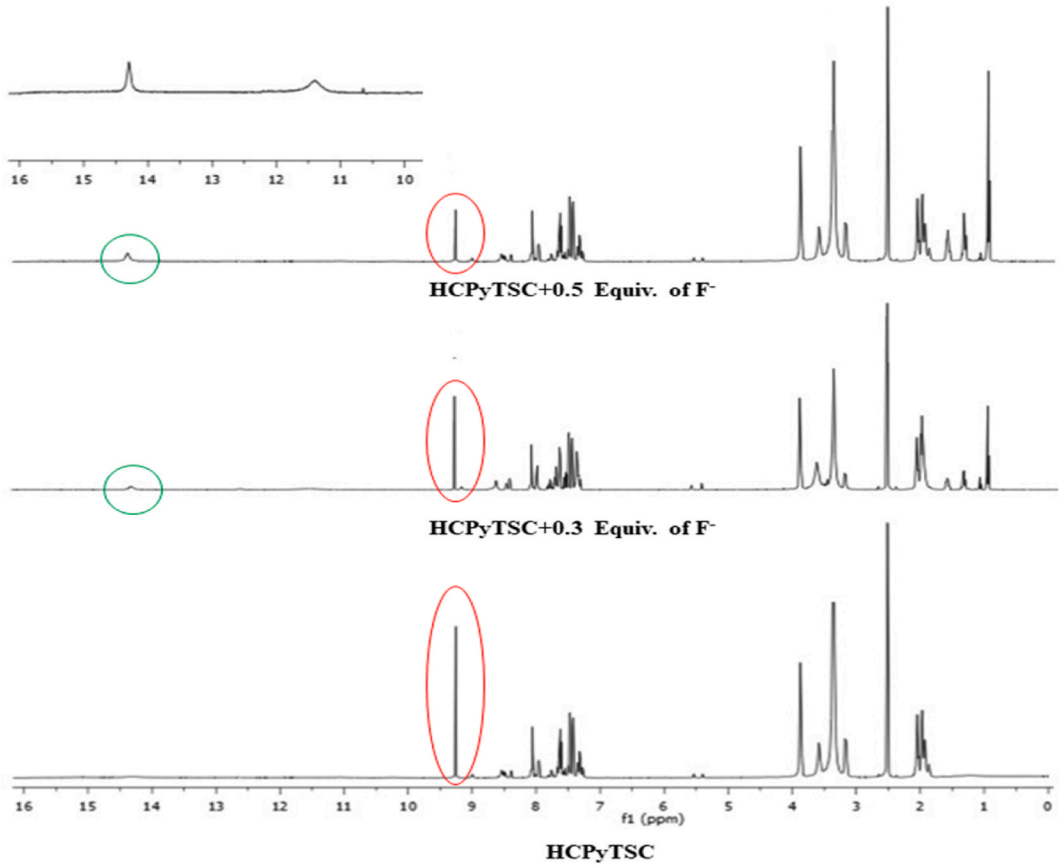

Fig. 10. ^{1}H NMR titration of HCPyTSC with different equivalents of fluoride ion. Inset: expansion of the region 10–16 ppm in the presence of 0.5 equivalents of TBAF.

ring. As seen in Fig. 10 adding 0.3–0.5 equivalents of fluoride ion causes the peak at 9.25 to decrease, which is due to C10–H10 forming a hydrogen bond with the strong electron negative fluoride ion. A new peak around 14.3 ppm in the ^{1}H NMR spectrum is clearly due to the unbound bifluoride ion $[HF_2]-$when 0.5 equiv. of fluoride was introduced. Initially, a fluoride ion forms a transient hydrogen-bonded complex with the H10 proton of the chemosensor HCPyTSC followed by deprotonation of H10 releasing HF which combines another F^- ion to give $[HF_2]^-$. At the same time, the peaks associated with the protons of the pyrrolidine and benzene rings exhibit no discernible shift in the ^{1}H NMR spectra, indicating that they were not engaged in the sensing process. Therefore, the decrease in intensity of the H10 proton and the emergence of a new peak in the ^{1}H NMR spectrum after the addition of fluoride ions to the chemosensor clearly suggest that the H10 proton was deprotonated.

3.9. CV titration

To further understand the way, the sensor HCPyTSC binds to Cu^{2+}, cyclic voltammetry (CV) studies were conducted in acetonitrile solution (Fig. 11). Cathodic peak current was observed in relation to a silver/silver chloride (Ag/AgCl) electrode by setting the scan rate to 0.1 Vs^{-1}. As working and counter electrodes, respectively, electrodes composed of glassy carbon (GC) and platinum were used. On the naked GC, no prominent redox peaks were visible, whereas one reduction peak for the HCPyTSC (1×10^{-3} M) was observed at Epc = 0.038 V on the cyclic voltammogram of the modified electrode (GC/HCPyTSC). This peak may have resulted from increased π-conjugation induced by the electronegative nitrogen atom. The newly formed redox peaks upon the addition of Cu^{2+} into the medium indicate the formation of the HCPyTSC-Cu complex. The formation of oxidation and reduction peaks at Epa = −0.135 V and Epc = 0.016 V ascribes the polarization of the C═N and C═S groups. The greater conductance of the Cu^{2+} ions might be the reason for the current increase brought on by the successive addition of Cu^{2+} ions to the sensor HCPyTSC. Therefore, these results demonstrate that the sensor HCPyTSC has a high affinity for binding Cu^{2+} ions.

4. Computational approaches

4.1. Geometry-optimized structures and molecular orbital analysis

The optimized structure of the chemosensor HCPyTSC was determined by DFT (B3LYP, 6-311G (d, p)) calculations. The optimized structure of the compound and experimentally determined crystal structure were depicted in Fig. 12A and B. The compound's anticipated (DFT) and experimental (XRD) bond parameters show good agreement (Table 2). In light of the accuracy of the projected compound structure, further theoretical research coupled with the computation of a few thermodynamic variables may be more reliable.

The various geometries of the receptor and its complex with fluoride and copper ions in the ground state and excited states have been thoroughly explored at the B3LYP/6-311G(d,p) and TD-DFT/CAM-B3LYP/6-311G(d, p) levels, respectively, to examine the fluoride and copper ions sensing mechanism. Fig. S15 displays the complex HCPyTSC-Cu^{2+} and the sensor HCPyTSC's optimized structures. HOMO-LUMO transitions of HCPyTSC along with the information on the nature of the first few excited states, their energies, and oscillator strengths are given in the supporting information file (Table S3). DFT calculations show that sensor HCPyTSC's electron density is primarily distributed on pyrazole nitrogens and thiocarbonyl units at HOMO and LUMO (Fig. S16). It also demonstrates that a significant ICT process occurs. The ICT process decreased when Cu^{2+} was added together with the pyrazole nitrogen unit of HCPyTSC, and the fluorescent signal was significantly enhanced. The charge density in the HOMO and LUMO energy levels was transferred from the sensor HCPyTSC to the Cu^{2+} ion when the Cu^{2+} ion was added. Thus, the finding demonstrates that a lone pair electron was transported from nitrogen atom to Cu^{2+} metal ion. As a result of this electron transfer, the ICT process in the sensor HCPyTSC decreases, which dramatically boosts fluorescence intensity.

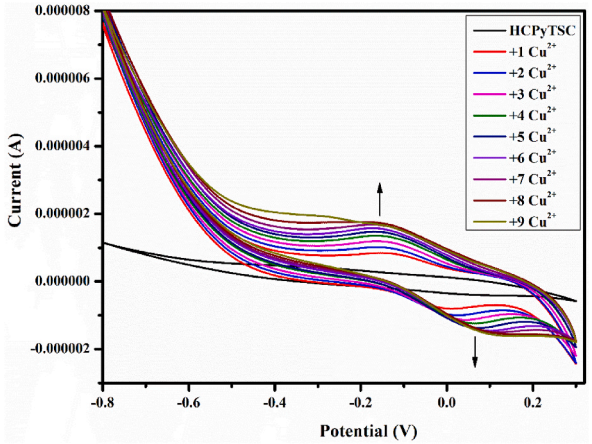

Fig. 11. Cyclic voltammetry of HCPyTSC (1×10^{-3} M) with Cu^{2+} (1×10^{-3} M) in acetonitrile potential range: −0.8 V up to 0.3 V, v = 0.1 V s^{-1}.

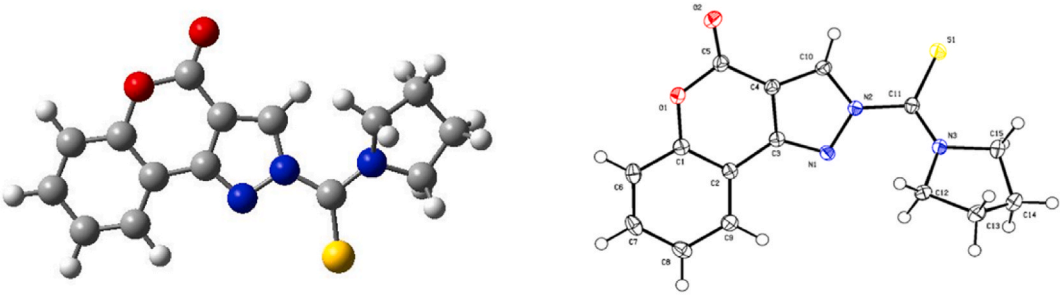

Fig. 12. Optimized (A) and single crystal XRD (B) structures of HCPyTSC.

Table 2
Selected bond lengths and bond angles of HCPyTSC (Predicted/Experimental).

Bond length (Å)	Bond angle (°)
DFT XRD	DFT XRD
S(1)–C(11) 1.70 1.67	C(3)-N(1)-N(2) 103.89 103.32
N(2)–N(1) 1.40 1.38	N(2)-C(10)-C(4) 106.41 105.74
N(2)–C(10) 1.37 1.35	N(2)-C(10)-H(10) 127.99 127.1
N(2)–C(11) 1.42 1.43	N(2)-C(11)-S(1) 119.19 118.84
N(3)–C(11) 1.33 1.32	N(3)-C(11)-S(1) 124.50 124.61
C(10)–H(10) 1.07 0.95	N(2)-C(11)-N(3) 116.30 116.55.

Generally, information about molecules' three-dimensional charge distributions is provided by the molecular electrostatic potential surface analysis. MEP exhibits major characteristics such as changes in dipole moment, size, electronegativity, electron density, partial charges, and chemical reactivity sites found in the molecule [43]. The regions on a molecule that are open to an electrophilic assault can therefore be effectively detected by MEP analysis since it displays the regions which are electron-rich and deficient in the molecules. This surface analysis makes it easier to see the molecules' variously charged areas, which are indicated by different colours. Fig. 13 shows the surface analysis outcome from the molecular electrostatic analysis. By analyzing the positive and negative charged electrostatic potential regions in the complex, a range of potential interactions in the molecules can be predicted. The surface with a high electrostatic potential, which is depicted by the colour blue, describes the absence of electrons or the partial positive charge that the molecule possesses. According to the MEP surface, the area close to the nitrogen and oxygen atoms is extremely vulnerable to electrophilic assaults. The possibility of a significant interaction between the Cu^{2+} ion and the nitrogen of the pyrazole ring in the sensor HCPyTSC is also considered in this paper.

4.2. *Transition state calculation*

To understand the dynamic nature of the hydrogen transfer reaction in the sensing process, we estimated Gibb's free energy profile for the sensing mechanism, and Fig. 14 illustrating the Gibb's free energy profile. The HCPyTSC- F^- complex has the Gibb's free energy of -8.73×10^5 kcal/mol corresponds to its ground state. Proton migration takes place between sensor HCPyTSC and fluoride anion. For HCPyTSC, the total change in Gibbs free energy during the reaction is exergonic by −7.13 kcal/mol. Less Gibbs free energy

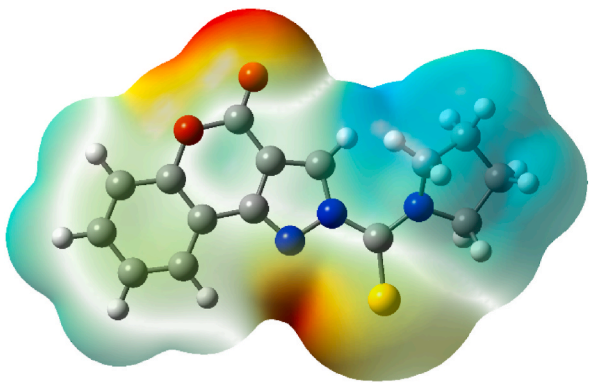

Fig. 13. The MEP of sensor HCPyTSC determined using B3LYP/6-311G (d, p) basis set.

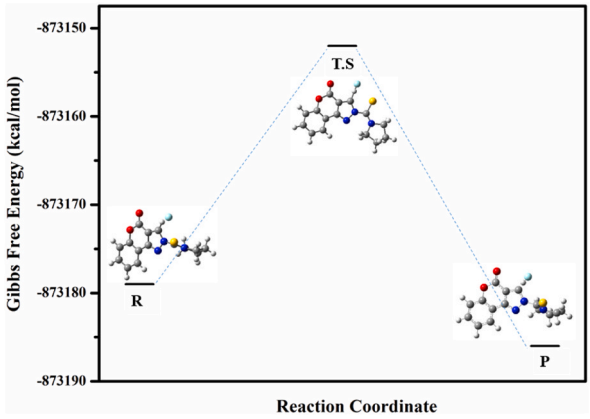

Fig. 14. Profiles of Gibb's free energy for the reaction mechanism. HCPyTSC-F^-: reactant (ground state); TS: transition state; HCPyTSC-F^-: product.

difference between reactant and product indicates that the reaction is reversible, which is the best support for the explanation of the chemosensing process. The Gibbs free energy value was further used to compute the binding constant of the sensing process, and it was discovered to be 1.70×10^5 M^{-1} for HCPyTSC, which was close to the experimental measurement. The intrinsic reaction coordinate (IRC) calculation for the transition state's optimized structure was carried out in order to confirm the process' intermediate production. IRC computation discovers an intermediate by relaxing the transition state toward the products, and frequency calculation later proved this intermediate.

4.3. Natural bond orbital (NBO) analysis

The investigation of intra- and intermolecular interactions may be improved by using data from natural bond orbital (NBO) studies, which provide insight into interactions in both filled and virtual orbital regions. The ground state (S0) and emission investigations of optimal geometries anticipate a proton transfer from C10 by changing the bond length between C10–H10 and F–H10. NBO calculations were done at the ground state of receptor-F (HCPyTSC- F^-) to aid in proton transport mechanism taking the place from C10–H10 rather than C12–H12 proton in the F^- ion chemosensing. From the electron donor orbital, acceptor orbital, and the interacting stabilization energy in the ground state the second perturbation energy has been calculated and used to predict the strength of the interaction between host and guest. Using this, we can explain the weak interaction. According to Equation (2), second order perturbation is defined as,

$$E(2) = \Delta E = \frac{q_i F_{ij}^2}{\varepsilon_j - \varepsilon_i} \tag{2}$$

Where q_i is the donor orbital occupancy, F_{ij} is the off-diagonal element in the NBO Fock matrix, E(2) is the second perturbation energy, and ε_i and ε_j are the orbital energies. Table 3 lists the principal interactions and their corresponding energy. The bond can be formed by the attractive interaction between F–H10, which was discovered in the ground of the HCPyTSC-F^- complex. The strong donor-acceptor interaction is confirmed by the substantial overlap of the electron density, which shows that the 'CH' proton in the pyrazole ring prefers to interact with the F^- ions rather than the 'CH' protons in the pyrrolidine ring (Fig. 15A). The ground state proton transport from the receptor is further supported by the NBO analysis with E(2). The possible complex formation between HCPyTSC and Cu^{2+} is further depicted in Fig. 15B.

5. Development of paper test kit

To boost the usability and convenience of the chemosensor HCPyTSC in fluoride ion detection, we integrated it into the tissue paper. The tissue paper (sheet Ply: 3 Ply, sheet size: 9.9 × 10.5 cm) strip was made by cutting it into the dimensions of 15 × 2 cm. As shown in Fig. 16, drops of the chemosensor HCPyTSC (1×10^{-3} M) was applied to tissue paper and dried in air. When fluoride ions were added to the developed paper kit in varying concentrations (1×10^{-5} M to 1×10^{-4} M), the colour of the paper altered from light yellow to dark red. The colour shades of the digital images were analysed using Photoshop (Adobe) to separate shades of yellow and red colours to a single-channel grayscale. These findings suggested that our chemosensor HCPyTSC may offer a promising method for detecting fluoride ions in drinking water using the naked eye.

6. Live cell image studies

It was investigated whether the coumarin-linked 1,2-pyrazole probe HCPyTSC could identify F^- in living T24 cells. Utilizing a calorimetric technique, the cytotoxicity of the sensor HCPyTSC was evaluated in T24 cells. After being treated with the sensor's

Table 3
The second-perturbation energy E(2) (kcal/mol) donor-acceptor interaction with respect to HCPyTSC-F^-.

Donor	Acceptor	Interaction	E2(kcal/mol)
HCPyTSC-F^- (Ground state)			
CR F	LP × H10	π-n*	10.55
LP F	LP × H10	n-n*	268.97
LP F	LP H12	n-n*	153.51

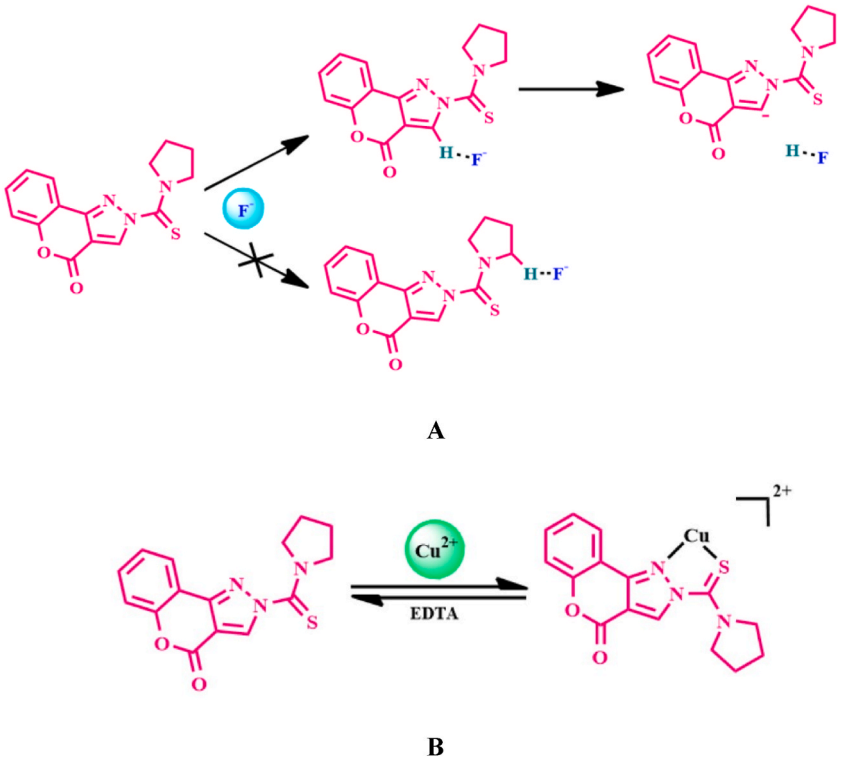

Fig. 15. The hypothesised sensing mechanisms of HCPyTSC employ the fluoride (A) and copper (B) ions.

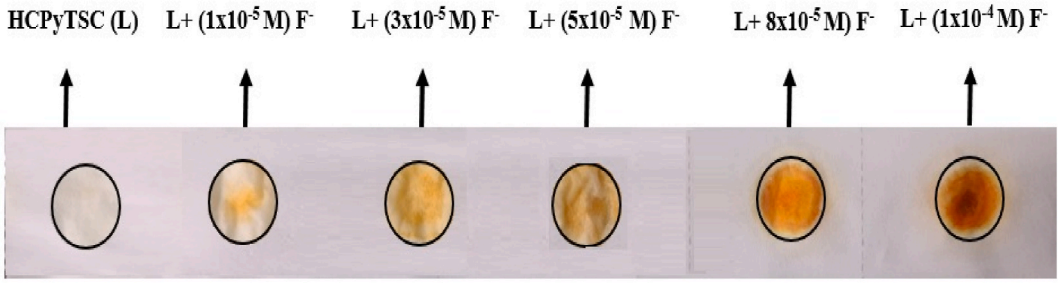

Fig. 16. The colour changes of tissue paper-based test kit upon the addition of various amounts of F^- ion.

solution, the bright-field image demonstrates that the T24 cells are viable throughout the live cell imaging trials, indicating that the probe is not hazardous to the cells. Confocal microscopy was used in a bioimaging examination to investigate the HCPyTSC-F^- complex's intracellular sensing. Three different concentrations of HCPyTSC were chosen: 0.671 μM, 0.340 μM, and 0.163 μM based on the results of the cell viability tests. There was no evidence of fluorescence in the cells after separate treatments with HCPyTSC and F^-. Notably, blue fluorescence was seen when HCPyTSC was given to the cells that had been exposed to F^- (Fig. 17). Images with fluorescence and bright field overlays demonstrated that HCPyTSC could penetrate cell walls and detect F^- in T24 cells' cytoplasm.

Additionally, the chemosensor HCPyTSC employed in this work is matched with other chemosensors that were recently reported (Table S1) [44–53]. The comparison investigation shows that the detection limit of the existing chemosensor HCPyTSC is significant. In

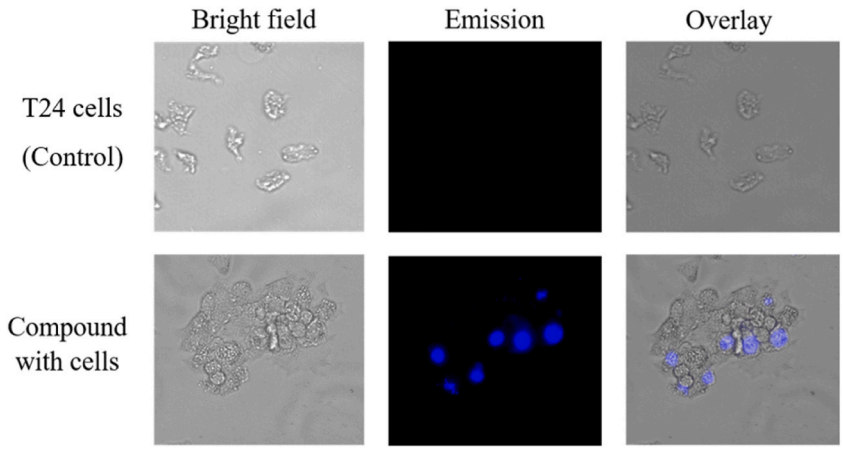

Fig. 17. T24 cell bio-imaging visualisation for F^- ion detection with HCPyTSC sensor.

the same way, the sensor performs better in studies involving fluorescent live-cell imaging. Due to its low LOD and lack of interference from other metal ions, the current chemosensor HCPyTSC is highlighted as having potential to play a more significant role in analytical chemistry.

7. Molecular logic gate

As was covered in earlier sections, the presence of different anionic and cationic inputs may have a significant impact on the UV–Vis

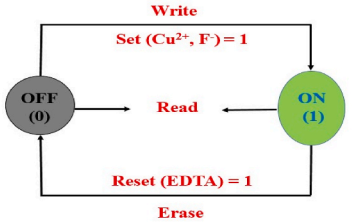

(A)

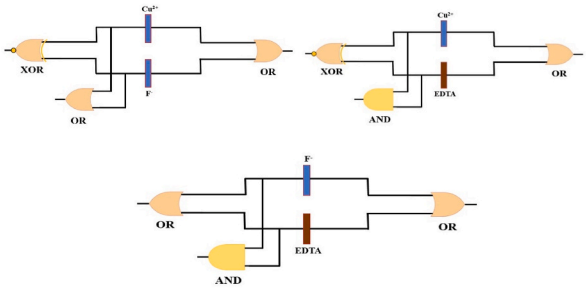

(B)

IN 1 Cu^{2+}	IN 2 F^-	IN 3 EDTA	OUT 1 Emission ON	OUT 2 Emission OFF
0	0	0	0	1
1	0	0	1	0
1	0	1	0	1
1	1	1	0	1
0	1	0	1	0
0	1	1	1	0
0	0	1	0	1

C

Fig. 18. A memory device with a loop and Write-Read-Erase-Read features is used to explain the reversible logic gate operations (A), logic gate circuit (B), and its truth table (C).

absorption and fluorescence spectra of HCPyTSC. Therefore, the many modes of interaction sparked our curiosity in building Boolean logic gates and doing calculations at the molecular level. Adding basic ions such as Cu^{2+} and F^{-} to the sensor in acetonitrile exhibit observable colour and fluorescence spectral alterations. A memory device with a loop and Write-Read-Erase-Read features is used to explain the reversible logic gate operations (Fig. 18A). We are interested in creating combinational logic gates using three ionic inputs while taking into account the emission output signals at suitable wavelengths. Of particular importance is a three-input majority gate. The ability of this gate to absorb and produce a substantial amount of information is its most important characteristic. Additionally, a three-input gate can be thought of as a flexible building block for creating circuits with more intricate design requirements. As shown in Fig. 18B, OR, XOR and logic gates are built at the molecular level employing F^{-}, Cu^{2+}, and EDTA as three chemical inputs, while monitoring the emission band at 476 and 492 nm as the output signal. In this case, in the absence of any inputs, the 476/492 nm emission intensity is less than a predetermined threshold level, implying the Boolean value of "0," while for the remaining three probable combinations, the emission is greater than the threshold denoting the Boolean value of "1" (Fig. 18C). These results suggest that HCPyTSC can play a key role in the creation of logic circuits in the domains of molecular electronics and nanotechnology.

8. Molecular keypad lock application

The sequence in which the inputs are applied determines the value of the output signal in various sorts of logical molecules known as "molecular keypad locks." It is a fluorescence sensor-based molecular electronics security application with great expectation for security based on molecular level information. The locks with keypad must be opened using a particular sequence of chemical inputs. Cu^{2+}, F^{-} and EDTA are combined with the chemosensor HCPyTSC to create a molecular lock that is depending on sequence. We chose four different input signals, denoted, respectively, as "L," "C," "F," and "E," which stood for HCPyTSC, Cu^{2+}, F^{-}, and EDTA. Furthermore, we generated the following eight input combinations: L, LC, LE, LF, LCE, LCF, LEF and LCEF. Compared to other combinations, the LC, LF and LEF combinations gave the highest fluorogenic output signal (Fig. 19). The molecular keypad is similar to an electronic keypad in that it includes multiple keys (A-Z), but only the right passwords (LC, LF and LEF) may unlock a locked object; all other possible arrangements are not valid.

9. Conclusion

A new coumarin-based 1,2-pyrazole based on pyrrolidine was created and then described. The compound's chemosensing activity was investigated theoretically and experimentally. Spectral changes can reveal the preferential sensing towards fluoride and copper ions. A new peak at 430 nm was formed after the F^{-} ion was added to HCPyTSC, suggesting that the HCPyTSC- F^{-} complex had formed. In comparison to Cu^{2+}, the chemosensor HCPyTSC exhibits higher binding affinity for the F^{-} ion. HCPyTSC displayed detection limits

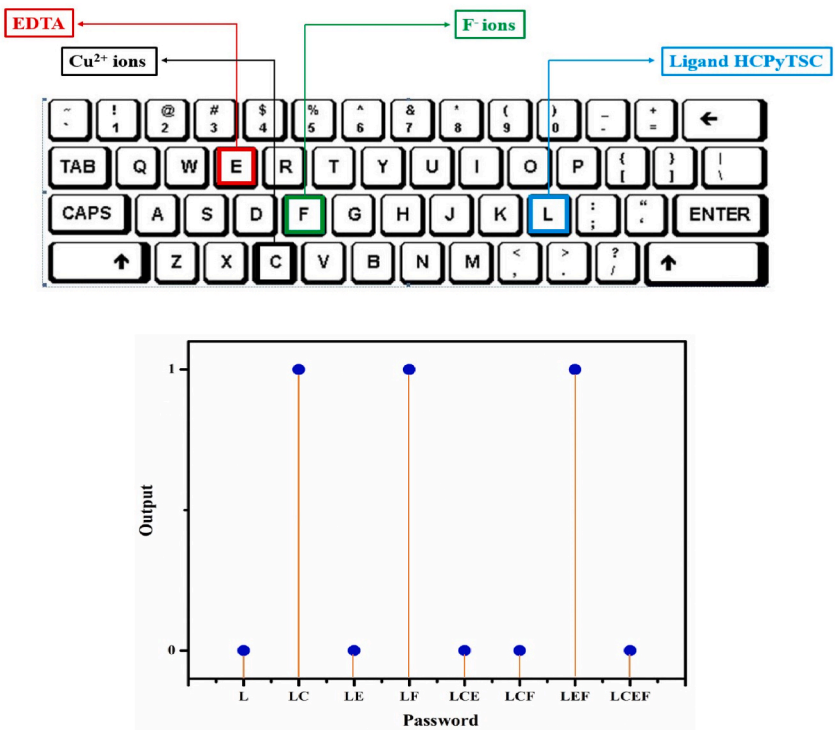

Fig. 19. When the correct password, which are LC, LF, and LEF, is entered, the constructed keypad lock at 476/492 nm is activated.

of 4.62 nM for F^- ions and 15.36 nM for Cu^{2+} ions. In an acetonitrile medium, the binding constants (Kb) were established as 2.06 × 105 M^{-1} for F^- ions and 1.88 × 105 M^{-1} for Cu^{2+} ions. The proposed sensing mechanism was shown in Fig. 16 to be thermodynamically permissible based on DFT and TD-DFT results. The F^- ion sensing mechanism by HCPyTSC was disclosed by the calculations for the transition and intermediate states. NBO analysis added more proof that the proton transition process existed. The second-order perturbation energy value confirms that the CH group of the pyrazole ring underwent hydrogen bonding and deprotonation rather than the CH group of the pyrrolidine ring. The experimental results were correctly interpreted by the DFT and TD-DFT studies, and deprotonation by fluoride ion can proceed to the ground state process. The theoretical and experimentally determined binding constants for F^- were in good agreement and supported the high fluoride chemosensing efficiency of HCPyTSC. Also, the chemosensor HCPyTSC exhibits emission and absorption responses that, when interacting with F^- and Cu^{2+} ions, can replicate the behavior of multiple logic gates, including AND, XOR, and OR gates. The paper-based sensor demonstrated superior efficacy in the detection of F^- ions compared to other anions. To assess the selective detection of F^- ions within living cells and evaluate its cell permeability, HCPyTSC was investigated through live-cell imaging in T24 cells.

CRediT authorship contribution statement

Puthiyavalappil Rasin: Writing - review & editing, Writing - original draft, Methodology, Investigation, Formal analysis, Data curation, Conceptualization. **Sabeel M. Basheer:** Methodology, Investigation, Data curation. **Jebiti Haribabu:** Validation, Methodology, Investigation, Funding acquisition, Formal analysis, Data curation. **K.N. Aneesrahman:** Investigation, Formal analysis, Data curation. **Vipin Manakkadan:** Methodology, Investigation, Data curation, Conceptualization. **Vishnunarayanan Namboothiri Vadakkedathu Palakkeezhillam:** Methodology, Investigation, Formal analysis, Data curation. **Nattamai Bhuvanesh:** Visualisation, Validation, Resources, Methodology, Investigation, Formal analysis, Data curation. **Cesar Echeverria:** Methodology, Investigation, Formal analysis, Data curation. **Juan F. Santibanez:** Methodology, Investigation, Formal analysis, Data curation. **Anandaram Sreekanth:** Validation, Supervision, Formal analysis, Conceptualization.

Declaration of competing interest

The authors declare that they have no known competing financial interests or personal relationships that could have appeared to influence the work reported in this paper.

Acknowledgements

The Ministry of Human Resource Development, Government of India, has my sincere gratitude for their financial assistance. For the instrumentation facilities, the author is grateful to the National Institute of Technology. Also, this research thanks the Regional Competitiveness (FIC Regional, 2023) of the Regional government of Atacama, code BIP 40049126-0, 40045259-0 and 40035624-0 for the financial support.

Supplementary materials

For the structures listed in this study, crystallographic data have been sent as extra publication numbers to the Cambridge Crystallographic Data Centre (CCDC) (2226857 respective for HCPyTSC).

Appendix A. Supplementary data

Supplementary data to this article can be found online at https://doi.org/10.1016/j.heliyon.2024.e24077.

References

[1] S. Shantanam, Mueller, 乳鼠心肌提取 HHS public access, Physiol. Behav. 176 (1) (2018) 139–148.
[2] P. Meshram, B.D. Pandey, Abhilash, Perspective of availability and sustainable recycling prospects of metals in rechargeable batteries – a Resource overview, Resour. Pol. 60 (October 2018) (2019) 9–22, https://doi.org/10.1016/j.resourpol.2018.11.015.
[3] N. Akobundu, A.; H. O., N. Evaluation of heavy metal in soils from enyimba dumpsite in Aba, Southeastern Nigeria using contamination factor and geo-accumulation index, Energy Environ. Res. 3 (1) (2013) 125–134, https://doi.org/10.5539/eer.v3n1p125.
[4] A. Verma, R. Kumar, S. Yadav, Distribution, pollution levels, toxicity, and health risk assessment of metals in surface dust from bhiwadi industrial area in North India, Hum. Ecol. Risk Assess. 26 (8) (2020) 2091–2111, https://doi.org/10.1080/10807039.2019.1650328.
[5] R.A. Festa, D.J. Thiele, Copper: an essential metal in biology copper in prokaryotes, Festa RA, Thiele DJ. Copp. An Essent. Met. Biol. Curr. Biol. 21 (21) (2011) 877–883, https://doi.org/10.1016/j.cub.2011.09.040.Copper.
[6] I. Khemiri, F. Tebbji, A. Sellam, Transcriptome analysis uncovers a link between copper metabolism, and both fungal fitness and antifungal sensitivity in the opportunistic yeast Candida albicans, Front. Microbiol. 11 (May) (2020) 1–13, https://doi.org/10.3389/fmicb.2020.00935.
[7] S. Sharma, K.S. Ghosh, Recent advances (2017–20) in the detection of copper ion by using fluorescence sensors working through transfer of photo-induced electron (PET), excited-state intramolecular proton (ESIPT) and förster resonance energy (FRET), Spectrochim. Acta Part A Mol. Biomol. Spectrosc. 254 (2021) 119610, https://doi.org/10.1016/j.saa.2021.119610.

[8] D.G. Lurie, J.M. Holden, A. Schubert, W.R. Wolf, N.J. Miller-Ihli, The copper content of foods based on a critical evaluation of published analytical data, J. Food Compos. Anal. 2 (4) (1989) 298–316, https://doi.org/10.1016/0889-1575(89)90002-1.

[9] S.D. Robinson, B. Cooper, T.V. Leday, Copper deficiency (hypocupremia) and pancytopenia late after gastric bypass surgery, Baylor Univ. Med. Cent. Proc. 26 (4) (2013) 382–386, https://doi.org/10.1080/08998280.2013.11929011.

[10] D.R. Coates, J.M. Chin, S.T.L. Chung, 基因的改变NIH public access, Bone 23 (1) (2011) 1–7, https://doi.org/10.1038/oby.2008.614.Acquired.

[11] A. Abusabeib, W. El Ansari, W. Elhag, First case report of acquired copper deficiency following revisional single anastomosis duodeno-ileal bypass with sleeve gastrectomy (SADI-S) leading to severe pancytopenia with refractory anemia, Obes. Surg. 30 (12) (2020) 5131–5134, https://doi.org/10.1007/s11695-020-04916-3.

[12] J.A. Ansari, M.K. Ahmad, A.K. Verma, N. Fatima, H.J. Khan, M. Waseem, A.R. Khan, A.A. Mahdi, P. Abbas, A. Mahdi, Microwave assisted determination of minerals and toxic metals in traditionally used medicinal plant zingiber officinale roscoe by inductively coupled plasma-optical emission spectrometer, Int. J. Adv. Res. 3 (4) (2015) 879–887.

[13] S.R. Jaiser, G.P. Winston, Copper deficiency myelopathy, J. Neurol. 257 (6) (2010) 869–881, https://doi.org/10.1007/s00415-010-5511-x.

[14] H.L. Tey, A practical classification of childhood hypopigmentation disorders, Acta Derm. Venereol. 90 (1) (2010) 6–11, https://doi.org/10.2340/00015555-0794.

[15] T. Hirayama, G.C. Van De Bittner, L.W. Gray, S. Lutsenko, C.J. Chang, Near-infrared fluorescent sensor for in vivo copper imaging in a murine Wilson disease model, Proc. Natl. Acad. Sci. U.S.A. 109 (7) (2012) 2228–2233, https://doi.org/10.1073/pnas.1113729109.

[16] J.F.B. Mercer, The molecular basis of copper-transport diseases, Trends Mol. Med. 7 (2) (2001) 64–69, https://doi.org/10.1016/S1471-4914(01)01920-7.

[17] S. Sharma, , Chayawan, J. Debnath, K. Sundar Ghosh, Method for highly selective, ultrasensitive fluorimetric detection of Cu2+ and Al3+ by Schiff bases containing o-phenylenediamine and o-aminophenol, Methods 217 (July) (2023) 27–35, https://doi.org/10.1016/j.ymeth.2023.06.013.

[18] S. Sharma, A. Bhattacharya, Drinking water contamination and treatment techniques, Appl. Water Sci. 7 (3) (2017) 1043–1067, https://doi.org/10.1007/s13201-016-0455-7.

[19] S. Sharma, K.S. Ghosh, Overview on recently reported fluorometric sensors for the detection of copper ion based on internal charge transfer (ICT), paramagnetic effect and aggregation induced emission (AIE) mechanisms, J. Mol. Struct. 1237 (2021) 130324, https://doi.org/10.1016/j.molstruc.2021.130324.

[20] A. Ghosh, K. Mukherjee, S.K. Ghosh, B. Saha, Sources and toxicity of fluoride in the environment, Res. Chem. Intermed. 39 (7) (2013) 2881–2915, https://doi.org/10.1007/s11164-012-0841-1.

[21] W. Qiao, Q. Liu, Z. Li, H. Zhang, Z. Chen, Changes in physicochemical and biological properties of porcine bone derived hydroxyapatite induced by the incorporation of fluoride, Sci. Technol. Adv. Mater. 18 (1) (2017) 110–121, https://doi.org/10.1080/14686996.2016.1263140.

[22] C. Bergman, D. Gray-Scott, J.J. Chen, S. Meacham, What is next for the dietary reference intakes for bone metabolism related nutrients beyond calcium: phosphorus, magnesium, vitamin D, and fluoride? Crit. Rev. Food Sci. Nutr. 49 (2) (2009) 136–144, https://doi.org/10.1080/10408390701764468.

[23] T. Perera, S. Ranasinghe, N. Alles, R. Waduge, Effect of fluoride on major organs with the different time of exposure in rats, Environ. Health Prev. Med. 23 (1) (2018) 1–9, https://doi.org/10.1186/s12199-018-0707-2.

[24] M. Bashash, M. Marchand, H. Hu, C. Till, E.A. Martinez-Mier, B.N. Sanchez, N. Basu, K.E. Peterson, R. Green, L. Schnaas, A. Mercado-García, M. Hernández-Avila, M.M. Téllez-Rojo, Prenatal fluoride exposure and attention deficit hyperactivity disorder (ADHD) symptoms in children at 6–12 years of age in Mexico city, Environ. Int. 121 (June) (2018) 658–666, https://doi.org/10.1016/j.envint.2018.09.017.

[25] K. Lund, J. Ekstrand, J. Boe, P. Søstrand, J. Kongerud, Exposure to hydrogen fluoride: an experimental study in humans of concentrations of fluoride in plasma, symptoms, and lung function, Occup. Environ. Med. 54 (1) (1997) 32–37, https://doi.org/10.1136/oem.54.1.32.

[26] E.A. Adkins, K. Yolton, J.R. Strawn, F. Lippert, P.H. Ryan, K.J. Brunst, Fluoride exposure during early adolescence and its association with internalizing symptoms, Environ. Res. 204 (PC) (2022) 112296, https://doi.org/10.1016/j.envres.2021.112296.

[27] S.M. Basheer, A.C. Willis, R.J. Pace, A. Sreekanth, Spectroscopic and TD-DFT studies on the turn-off fluorescent chemosensor based on anthraldehyde N(4) cyclohexyl thiosemicarbazone for the selective recognition of fluoride and copper ions, Polyhedron 109 (2016) 7–18, https://doi.org/10.1016/j.poly.2016.01.021.

[28] N. Kaur, G. Kaur, U.A. Fegade, A. Singh, S.K. Sahoo, A.S. Kuwar, N. Singh, Anion sensing with chemosensors having multiple –NH recognition units, TrAC, Trends Anal. Chem. 95 (2017) 86–109, https://doi.org/10.1016/j.trac.2017.08.003.

[29] D.N.A. Boobbyer, P.J. Goodford, P.M. Mcwhinnie, R.C. Wade, New hydrogen-bond potentials for use in determining energetically favorable binding sites on molecules of known structure, J. Med. Chem. 32 (5) (1989) 1083–1094, https://doi.org/10.1021/jm00125a025.

[30] D. Cao, Z. Liu, P. Verwilst, S. Koo, P. Jangjili, J.S. Kim, W. Lin, Coumarin-based small-molecule fluorescent chemosensors, Chem. Rev. 119 (2019) 10403–10519, https://doi.org/10.1021/acs.chemrev.9b00145.

[31] G. Tian, Z. Zhang, H. Li, D. Li, X. Wang, D. Li, X. Wang, Critical reviews in analytical chemistry design , synthesis and application in analytical chemistry of photo-sensitive probes based on coumarin design , synthesis and application in analytical chemistry of photo-sensitive probes based on coumarin, Crit. Rev. Anal. Chem. 51 (6) (2021) 565–581, https://doi.org/10.1080/10408347.2020.1753163.

[32] K. Singh, S. Ralhan, P.K. Sharma, S.N. Dhawan, Vilsmeier-haack reaction on hydrazones: a convenient synthesis of 4-formylpyrazoles, J. Chem. Res. 5 (2005) 316–318, https://doi.org/10.3184/0308234054323959.

[33] H.M. Johnston, P.M. Palacios, B.S. Pierce, K.N. Green, Spectroscopic and solid-state evaluations of tetra-aza macrocyclic cobalt complexes with parallels to the classic cobalt(II) chloride equilibrium, J. Coord. Chem. 69 (11–13) (2016) 1979–1989, https://doi.org/10.1080/00958972.2016.1191630.

[34] M. Mohanbabu, P.N. Sathishkumar, N.S.P. Bhuvanesh, R. Karvembu, K. Saravanan, E. Vinoth, S. Aravindhan, Synthesis, characterization, crystal structure, hirshfeld surface analysis and DFT calculations of N-(Pyridin-2-Ylmethyl)Furan-2-Carboxamide and its molecular docking, J. Mater. Sci. Mater. Electron. 33 (12) (2022) 9616–9628, https://doi.org/10.1007/s10854-021-07601-y.

[35] P. Rasin, V. Manakkadan, V.N. Vadakkedathu Palakkeezhillam, J. Haribabu, C. Echeverria, A. Sreekanth, Simple fluorescence sensing approach for selective detection of Fe3+Ions: live-cell imaging and logic gate functioning, ACS Omega 7 (37) (2022) 33248–33257, https://doi.org/10.1021/acsomega.2c03718.

[36] A. Van Tonder, A.M. Joubert, A.D. Cromarty, Limitations of the 3-(4,5-dimethylthiazol-2-yl)-2,5-diphenyl-2H-tetrazolium bromide (MTT) assay when compared to three commonly used cell enumeration assays, BMC Res. Notes 8 (1) (2015), https://doi.org/10.1186/s13104-015-1000-8.

[37] S. Ganapathy-Kanniappan, J.F.H. Geschwind, R. Kunjithapatham, M. Buijs, L.H. Syed, P.P. Rao, S. Ota, M. Vali, The pyruvic acid analog 3-bromopyruvate interferes with the tetrazolium reagent MTS in the evaluation of cytotoxicity, Assay Drug Dev. Technol. 8 (2) (2010) 258–262, https://doi.org/10.1089/adt.2009.0226.

[38] D. Vejselova, H.M. Kutlu, Inhibitory effects of salicylic acid on A549 human lung adenocarcinoma cell viability, Turkish J. Biol. 39 (1) (2015) 1–5, https://doi.org/10.3906/biy-1401-7.

[39] S. Saranya, J. Haribabu, V.N. Vadakkedathu Palakkeezhillam, P. Jerome, K. Gomathi, K.K. Rao, V.H. Hara Surendra Babu, R. Karvembu, D. Gayathri, Molecular structures, hirshfeld analysis and biological investigations of isatin based thiosemicarbazones, J. Mol. Struct. 1198 (2019) 126904, https://doi.org/10.1016/j.molstruc.2019.126904.

[40] V.N.V. Palakkeezhillam, J. Haribabu, V. Manakkadan, P. Rasin, R.E. Varughese, D. Gayathri, N. Bhuvanesh, C. Echeverria, A. Sreekanth, Synthesis, spectroscopic characterizations, single crystal X-ray analysis, DFT calculations, in vitro biological evaluation and in silico evaluation studies of thiosemicarbazones based 1,3,4-thiadiazoles, J. Mol. Struct. (2023) 1273, https://doi.org/10.1016/j.molstruc.2022.134309.

[41] M. Oubaha, R. Copperwhite, R. Touch, A. Ovsianikov, R. Kiyan, Influence of hybrid organic – inorganic sol – gel matrices on the photophysics of amino-functionalized UV-sensitizers, J. Mater. Sci. 46 (February 2014) (2011) 400–408, https://doi.org/10.1007/s10853-010-4853-1.

[42] A. Pandith, K.R. Bhattarai, R.K. Guralamatta Siddappa, H.J. Chae, Y.J. Seo, Novel fluorescent C2-symmetric sequential on-off-on switch for Cu2+ and pyrophosphate and its application in monitoring of endogenous alkaline phosphatase activity, Sensor. Actuator. B Chem. 282 (November 2018) (2019) 730–742, https://doi.org/10.1016/j.snb.2018.11.111.

[43] P. Rasin, M.M. Mathew, V. Manakkadan, V.N.V. Palakkeezhillam, A. Sreekanth, A highly fluorescent pyrene-based sensor for selective detection of Fe3+ ion in aqueous medium: computational investigations, J. Fluoresc. 32 (3) (2022) 1229–1238, https://doi.org/10.1007/s10895-022-02940-3.

[44] Y. Wang, H. Wu, W.N. Wu, S.J. Li, Z.H. Xu, Z.Q. Xu, Y.C. Fan, X.L. Zhao, B.Z. Liu, An AIRE active Schiff base bearing coumarin and pyrrole unit: Cu2+ detection in either solution or aggregation states, Sensor. Actuator. B Chem. 260 (2018) 106–115, https://doi.org/10.1016/j.snb.2017.12.201.
[45] Z.G. Wang, X.J. Ding, Y.Y. Huang, X.J. Yan, B. Ding, Q.Z. Li, C.Z. Xie, J.Y. Xu, The development of coumarin Schiff base system applied as highly selective fluorescent/colorimetric probes for Cu2+ and tumor biomarker glutathione detection, Dyes Pigments 175 (2020), https://doi.org/10.1016/j.dyepig.2019.108156.
[46] H.S. Jung, P.S. Kwon, J.W. Lee, J.I.I. Kim, C.S. Hong, J.W. Kim, S. Yan, J.Y. Lee, J.H. Lee, T. Joo, J.S. Kim, Coumarin-derived Cu2+-selective fluorescence sensor: synthesis, mechanisms, and applications in living cells, J. Am. Chem. Soc. 131 (5) (2009) 2008–2012, https://doi.org/10.1021/ja808611d.
[47] W. Wang, W.J. Yuan, Q.L. Liu, Y.N. Lei, S. Qi, Y. Gao, Selective fluorescence sensor for Cu2+ with a novel triazole schiff-base derivative with coumarin units, Heterocycl. Commun. 20 (5) (2014) 289–292, https://doi.org/10.1515/hc-2014-0117.
[48] Y. Wang, X. Hao, L. Liang, L. Gao, X. Ren, Y. Wu, H. Zhao, A coumarin-containing Schiff base fluorescent probe with AIE effect for the copper(Ii) ion, RSC Adv. 10 (10) (2020) 6109–6113, https://doi.org/10.1039/c9ra10632d.
[49] W.H. Ding, D. Wang, X.J. Zheng, W.J. Ding, J.Q. Zheng, W.H. Mu, W. Cao, L.P. Jin, A turn-on fluorescence chemosensor for Al3+, F- and CN- ions, and its application in cell imaging, Sensor. Actuator. B Chem. 209 (2015) 359–367, https://doi.org/10.1016/j.snb.2014.11.144.
[50] S.K. Padhan, M.B. Podh, P.K. Sahu, S.N. Sahu, Optical discrimination of fluoride and cyanide ions by coumarin-salicylidene based chromofluorescent probes in organic and aqueous medium, Sensor. Actuator. B Chem. 255 (2018) 1376–1390, https://doi.org/10.1016/j.snb.2017.08.133.
[51] G.G.V. Kumar, M.P. Kesavan, G. Sivaraman, J. Rajesh, Colorimetric and NIR fluorescence receptors for F− ion detection in aqueous condition and its live cell imaging, Sensor. Actuator. B Chem. 255 (2018) 3194–3206, https://doi.org/10.1016/j.snb.2017.09.145.
[52] S.M. Basheer, A.C. Willis, A. Sreekanth, Spectroscopic and TD-DFT studies on the dual mode fluorescent chemosensors based on pyrene thiosemicarbazones, and its application as molecular-scale logic devices, J. Lumin. 183 (2017) 266–280, https://doi.org/10.1016/j.jlumin.2016.11.055.
[53] M. Iniya, D. Jeyanthi, K. Krishnaveni, D. Chellappa, A bifunctional chromogenic and fluorogenic probe for F- and Al3+ based on azo-benzimidazole conjugate, J. Lumin. 157 (2015) 383–389, https://doi.org/10.1016/j.jlumin.2014.09.018.